Synthesis, Characterization, Antibacterial, Antifungal, Antioxidant, and Anticancer Activities of Nickel-Doped Hydroxyapatite Nanoparticles

Saleth Sebastiammal [1,*], Arul Sigamani Lesly Fathima [1], Johnson Henry [2], Mohammad Ahmad Wadaan [3], Shahid Mahboob [3], Arwa Mohammad Wadaan [4], Irfan Manzoor [5], Kasi Gopinath [6], Mohan Rajeswary [7] and Marimuthu Govindarajan [8,9,*]

[1] Research Department of Physics, Holy Cross College (Autonomous), Nagercoil 629004, Tamil Nadu, India. (Affiliated to Manonmaniam Sundaranar University, Tirunelveli 627012, Tamil Nadu, India

[2] Department of Physics, Manonmaniam Sundaranar University, Tirunelveli 627012, Tamil Nadu, India

[3] Department of Zoology, College of Science, King Saud University, Riyadh 11451, Saudi Arabia

[4] College of Medicine, AlMaarefa University, Dariyah 13713, Saudi Arabia

[5] Department of Biology, Indiana University Bloomington, Bloomington, IN 47405, USA

[6] Division of Packaging Technology, Faculty of Agro-Industry, Chiang Mai University, Chiang Mai 50200, Thailand

[7] PG and Research Department of Zoology, ADM College for Women (Autonomous), Nagapattinam 611 001, Tamil Nadu, India

[8] Unit of Vector Control, Phytochemistry and Nanotechnology, Department of Zoology, Annamalai University, Annamalainagar 608 002, Tamil Nadu, India

[9] Unit of Natural Products and Nanotechnology, Department of Zoology, Government College for Women (Autonomous), Kumbakonam 612 001, Tamil Nadu, India

* Correspondence: sebastiammal.s@holycrossngl.edu (S.S.); drgovind1979@gmail.com or dr.m.govindarajan@gcwk.ac.in (M.G.); Tel.: +91-9585265999 (M.G.)

Abstract: The purpose of this research was to investigate the possible antibacterial, antifungal, antioxidant, and anticancer effects of nickel (Ni^{2+})-doped hydroxyapatite (HAp) nanoparticles (NPs) synthesized using the sol–gel approach. X-ray powder diffraction (XRD), Fourier transform infrared spectroscopy (FTIR), Raman spectroscopy (Raman), field-emission scanning electron microscopy (FESEM), and elemental analysis were used to characterize the Ni^{2+}-doped HApNPs. X-ray diffraction investigation showed that the nanoscale structure of Ni^{2+}-doped HApNPs was hexagonal, with an average crystallite size of 39.91 nm. Ni^{2+}-doped HApNPs were found to be almost spherical in form and 40–50 nm in size, as determined by FESEM analysis. According to EDAX, the atomic percentages of Ca, O, P, and Ni were 20.93, 65.21, 13.32, and 0.55, respectively. Ni^{2+}-doped HApNPs exhibited substantial antibacterial properties when tested in vitro against several pathogens, including *Escherichia coli*, *Shigella flexneri*, *Klebsiella pneumoniae*, *Pseudomonas aeruginosa*, and *Staphylococcus aureus*. Antibacterial activity, at 50 mg tested concentration, demonstrated superior effects on G^{-ve} bacteria than G^{+ve} pathogens. The antifungal activity of *Oidium caricae*, *Aspergillus flavus*, and *A. niger* revealed a zone of inhibition of 23, 11, and 5 mm, respectively. These actions rely on the organism's cell wall structure, size, and shape. Incorporating Ni^{2+} into HApNPs allows them to function as powerful antioxidants. Ni^{2+}-doped HApNPs had a good cytotoxic impact against the HeLa cell line, which improved with increasing concentration and was detected at a 68.81 µg/mL dosage. According to the findings of this study, the Ni^{2+}-doped HApNPs are extremely promising biologically active candidates owing to their improved functional features.

Keywords: green synthesis; bionanomaterials; hydroxyapatite; antimicrobial activity; cytotoxic effect; HeLa cell line

1. Introduction

Nanotechnology studies have expanded exponentially during the last three decades. Due to their large surface area concerning their volume, nanoparticles (NPs) have found applications across disciplines [1]. Its primary focus was on three major fields: energy, medicine, and agriculture [2]. The size and shape of nanoparticles might vary because they are synthesized using different methods. It works as intended in the common usages. The necessary size regulation of nanoparticles is achieved by using anionic and cationic surfactants [3]. In physical, chemical, and green synthesis [4,5], controlling nanoparticle size has been accomplished in several ways.

Much attention has been paid to incorporating 3d transition metals like Fe, Mn, and Co into HAP to increase their strength. The formation of the material and its physicochemical characteristics are affected by the doping procedure's annealing temperature grating. With the metal doping procedure, HAp nanopowder with Fe- and Co-doping exhibited improved antibacterial activity against *Shigella dysenteriae,* while HAp nanopowder with Mn doping showed more significant antibacterial activity against *Staphylococcus aureus*. Size, shape, stability, ion-releasing capacity, and the structure of the bacterial cell wall all play a role in the antibacterial activity of metal-doped HAp nanopowder [5].

Several metal nanoparticles are very effective antibacterial agents [6,7]. On the other hand, their prohibitive price prevents widespread commercial use. Therefore, it is important to work on finding alternatives that do not rely on noble metals for their economic viability. The inorganic mineral hydroxyapatite (HAp) is the principal structural component of teeth and bones [8,9], which makes it an attractive candidate in the quest for novel materials. The calcium phosphate in HAp is vitrified and ceramicist [10]. Calcium orthophosphate is a vital calcium potential in all living things. There are more options in dentistry, bone-tissue engineering, dental implant coating, orthopedics, and prosthetics [11,12].

For the most part, researchers have examined calcium-poor apatites, which may include divalent ion replacements. Several biological uses [10,13] are selected for HAp $[Ca_{10}(PO_4)_6OH_2]$, including antibacterial, drug delivery, dental, and orthopedic. When metal ions were present, the activity of Ca-HAp and its nitrate salt returned to normal. Because of its high mechanical strength and resistance to corrosion, Ni^{2+} is widely used as an orthopedic implant [14]. This element is also essential for all chordate organs. Ni^{2+} may replace Ca^{2+} in HAp without compromising the compound's crystalline structure. Researchers examined how adding Ni^{2+} to HApNPs preparation changed the final solid solution. Highly crystalline Ni^{2+}-doped HApNPs may be produced by sol–gel synthesis [15] by keeping these critical characteristics under controlled conditions. The present work describes the sol–gel synthesis of Ni^{2+}-doped HApNPs. Characterization of Ni^{2+}-doped HApNPs was performed using XRD, FTIR, Raman, FESEM, and EDAX. In addition, the antimicrobial, antioxidant, and antitumor properties were investigated.

2. Materials and Methods

2.1. Materials

In order to create Ni^{2+}-doped HAp nanoparticles, we mixed together $Ni(NO_3)_2.6H_2O$, $Ca(NO_3)_2.4H_2O$, PEG, NH_3, and $(NH_4)2HPO_4$. All chemicals used in this study were bought from Sigma-Aldrich, USA and were of reagent grade (99.9% purity). From Hi-Media in India, we procured Luria Bertani agar, potato dextrose agar, clotrimazole, and amikacin. Triple-distilled water was utilized in the experiments. The bacterial strains of *Shigella flexneri* (MTCC 1457), *Escherichia coli* (MTCC 40), *Pseudomonas aeruginosa* (MTCC 2642), *Klebsiella pneumoniae* (MTCC 432), and *Staphylococcus aureus* (MTCC 1935), as well as the fungal strains of *Oidium caricae*, *Aspergillus flavus*, and *A. niger*, were all obtained from KRIND Institute of Research and Development, Trichy, Tamil Nadu, India.

2.2. Preparation of PEG-Assisted Ni^{2+} doped HAp

Synthesis of PEG-assisted Ni^{2+}-doped HApNPs included employing double-distilled water, ammonia solution, di-ammonium hydrogen phosphate, nickel nitrate, and calcium

nitrate. Calcium nitrate, at 0.9 M, and nickel nitrate, at 0.1 M, were each diluted in 50 mL of distilled water and stirred with a magnetic stirrer for 30 min. In 50 mL of sterile water, 0.1 M PEG surfactant was combined with 0.1 M calcium and 0.1 M nickel solutions. A 0.6 M concentration of Di-ammonium hydrogen phosphate was achieved by dissolving the compound in the earlier solution. We slowly added the ammonia solution to the first combination, reaching a pH of 10. After draining in a hot air oven, the product was calcined for 2 h at 500 °C.

2.3. Antimicrobial Activity

Synthesized Ni^{2+}-doped HApNPs at a concentration of 50 g were tested for their antibacterial efficacy against five bacterial and three fungal strains [16]. Luria Bertani medium (pH 7.4) for bacteria and potato dextrose medium (pH 7.4) for fungi were used to incubate the test organisms at 37 °C for 18 to 24 h. Wells were drilled into the exterior of the sterile gel made of agar. Afterward, the triplicate plates were protected against bacteria and fungus. The five most frequent bacteria that cause infections are *Staphylococcus flexneri* (MTCC 1457), *Escherichia coli* (MTCC 40), *Pseudomonas aeruginosa* (MTCC 2642), *Klebsiella pneumoniae* (MTCC 432), and *Staphylococcus aureus* (MTCC 1935). *Oidium caricae*, *Aspergillus flavus*, and *A. niger* were used in tests to determine the antifungal activity. Positive control for bacteria and fungi was 30 g of amikacin and 10 g of clotrimazole, while DMSO served as a negative control.

2.4. Antioxidant Activity

Ni^{2+}-doped HApNPs' antioxidant ability was evaluated using DPPH and radical scavenging, as described by Brand-Williams et al. [17]. Hydrogen donation or free radical scavenging capacity of Ni^{2+}-doped HApNPs formed the basis for their antioxidant action. Scavenging of the products was also quantified with the use of the following equation:

$$\text{DPPH scavenging activity } (\%) = \frac{(\text{Abs control} - \text{Abs sample})}{(\text{Abs control})} \times 100$$

2.5. Anticancer Activity

Ni^{2+}-doped HApNPs were investigated for cytotoxicity against HeLa cells using a MTT assay. The HeLa cells came from the National Centre for Cell Sciences (NCCS) in Pune, India. In a humidified incubator (5% CO_2, 37 °C; Galaxy® 170 Eppendorf, Germany), tissues were principally grown in a 25 cm^2 tissue culture flask (DMEM in Himedia). The cell viability was examined visually using an inverted phase-contrast microscope.

3. Results and Discussion

3.1. XRD Analysis

Ni^{2+}-doped HApNPs exhibit a crystalline phase in the form of hexagonal HApNPs with well-defined diffraction peaks in the conventional X-ray diffraction (XRD) pattern (JCPDS: 09-0432), as shown in Figure 1. Hexagonal HApNPs doped with Ni^{2+} have been shown to have a P63/m space group. At 2θ = 26.61°, 27.93°, 28.87°, 31.21°, 32.58°, 34.50°, 40.59°, 47.16°, and 53.15°, diffraction peaks were seen that corresponded to the (002), (102), (210), (211), (300), (202), (221), (312), and (004) planes, respectively. Significantly, the crystal system is unaffected by the PEG surfactant.

The absence of a secondary phase for a nickel or any other impurity demonstrates that nickel ions have efficiently replaced calcium ions without modifying the crystal structure of HApNPs. The results of this study are in close accord with those of the previous studies [18–23]. When Ni^{2+} ions were replaced for specific Ca^{2+} sites, however, the dopant was substantially absorbed into the HApNPs lattice, as shown by a slight change in 2θ and distortion in the lattice cell properties. Using the more distinct diffraction peaks at the (102), (211), and (202) planes, we were able to calculate that the crystallite size is around 39.91 nm. Nevertheless, research shows that when Mg is replaced with Ca in stoichiometric

HApNPs, the lattice parameters decrease, and the peaks shift toward the lower diffraction angle [24,25]. Adsorption of the remaining Mg prevented additional grain formation onto the surface of the HApNPs, despite the HAp-Mg complex constantly producing random grains [26].
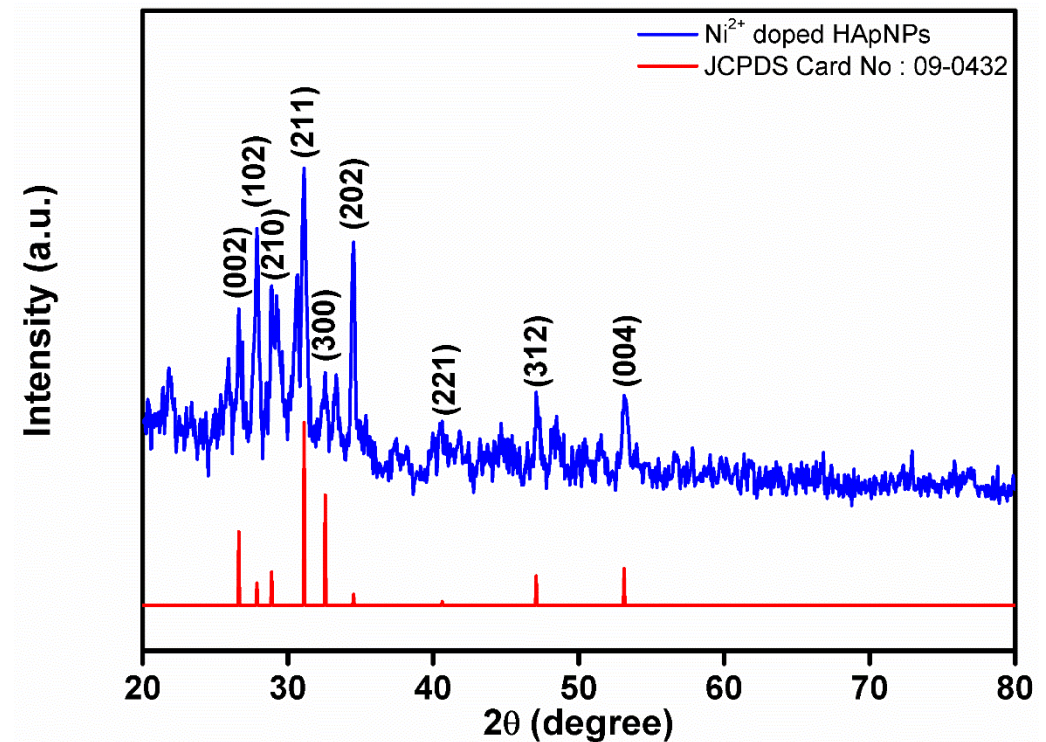

Figure 1. XRD analysis of Ni^{2+}-doped HApNPs calcined at 500 °C.

3.2. FTIR Analysis

Figure 2 depicts the FTIR spectrum of Ni^{2+}-doped HApNPs. Frequencies of 558 cm^{-1} and 608 cm^{-1} were assigned as the O-P-O bending mode. The 1040–1140 cm^{-1} range contains bands with a high intensity that have been assigned to the v3 asymmetric stretching mode of O-P-O. The presence of v3 carbonate ions (CO_3^{-2}) from the environment during sample preparation has been connected to the weak bands identified at 1460 cm^{-1}. However, the band at 1634 cm^{-1} is easily explained due to the lattice's two H_2O, H-O-H bending modes. It has been determined that the OH stretching contributes mild intensity to the appearance of two bands in the HApNPs, one wide at 3452 cm^{-1} and the other sharp at 3575 cm^{-1}. Water in the lattice, rather than absorbed water, is responsible for the persistence of the OH bands even at elevated temperatures. After all, at temperatures over 100 °C, absorbed moisture is evaporated. XRD analyses corroborate these results, suggesting that Ni^{2+} ions are present in the HAp structure.

Similar FTIR investigations showed that hydroxyl and phosphate functional groups were present in HAp and Mg-HAp, as indicated by the presence of characteristic sharp lines at 1026 cm^{-1} and 1032 cm^{-1}, respectively, and also showed that the phosphate groups stretched in a certain way [9]. According to an ongoing investigation, FTIR analysis confirms the presence of the PO_4^{3-} group in HAp, with peaks for HAp ranging from 1749 to 1736 cm^{-1}. In contrast, Mg-HAp formed a covalent bond with the absorbed water molecule [27]. In addition, the small peak at 969 cm^{-1} indicates symmetric stretching vibrations, which are often linked to a P-O mode [28]. The O-H bond is responsible for weak peaks at 3571 cm^{-1} for HAp and 3554 cm^{-1} for Mg-HAp. HAp and Mg-HAp exhibit a sizable stretching band around 1367 cm^{-1} [29], which may be traced back to the carbonate group. Most of this peak is due to the O-H stretching vibration in HAp.
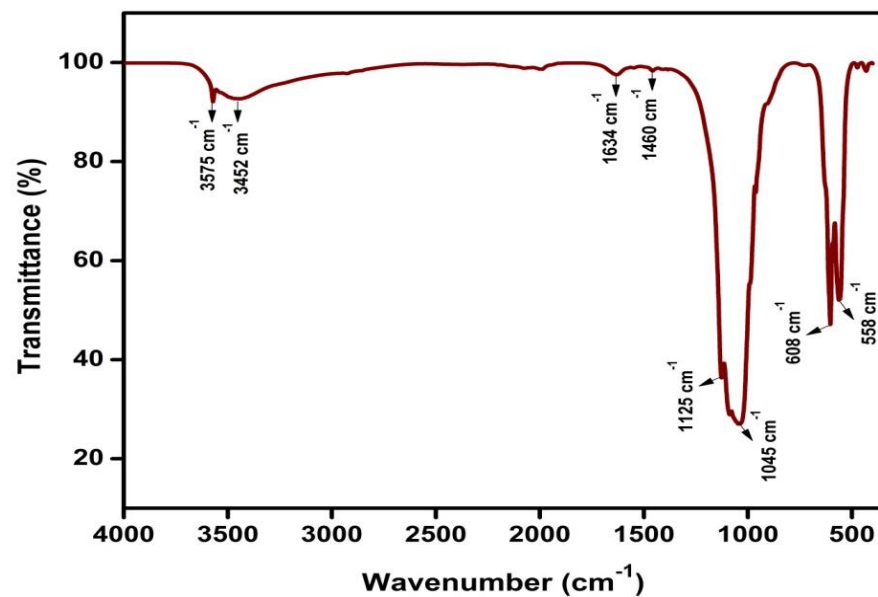
Figure 2. FTIR spectrum of Ni^{2+}-doped HApNPs calcined at 500 °C.

3.3. Raman Spectrum Analysis

Figure 3 illustrates the Raman spectrum of Ni^{2+}-doped HApNPs. Raman spectra of Ni^{2+}-doped HApNPs revealed vibrational bands related to phosphate group stretching and twisting modes. Most significantly, at 961 cm^{-1}, the symmetric stretching way of PO_4^{3-} (v1)—one can always recognize this peak as belonging to HApNPs. The low-intensity band at 363, 407, and 480 cm^{-1} is responsible for the bending behavior of PO_4^{3-} (v2symmetric). In this investigation, a band at 614 cm^{-1}, estimated at around 591 cm^{-1}, matches the irregular bending style of PO_4^{3-} (v2). It has been determined that the band saw at 1043 and 1163 cm^{-1} in the Raman spectra of Ni^{2+}-doped HApNPs is due to mild PO_4^{3-} (v3) stretching. There is strong agreement between our findings and the previously published values [5].
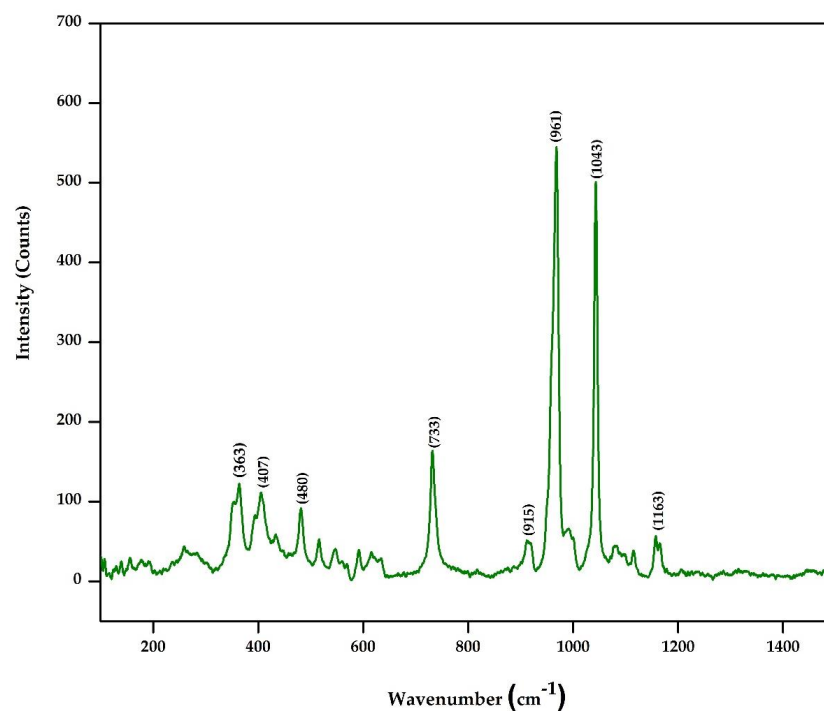

Figure 3. Raman spectrum of Ni^{2+}-doped HApNPs calcined at 500 °C.

3.4. FESEM Analysis

The morphology of the Ni^{2+}-doped HApNPs was studied by utilizing FESEM. FESEM images of Ni^{2+}-doped HApNPs are shown in Figure 4a,b at different magnifications. The particles have a spherical form and exhibit intense aggregation; their average size is 45 nm, and their length is 40–50 nm. The size-variant spherical and near-spherical shape was observed in Ni^{2+}-doped HApNPs. Agglomerated spherical NPs of about 50 nm in size resulted from an initial pH held constant at 10. The Ni^{2+}-doped HApNPs in the FESEM fit the XRD pattern nicely. This work shows that doping nano-hydroxyapatites with Ni^{2+} does not significantly alter their crystal structure but substantially reduces their crystallinity [30].
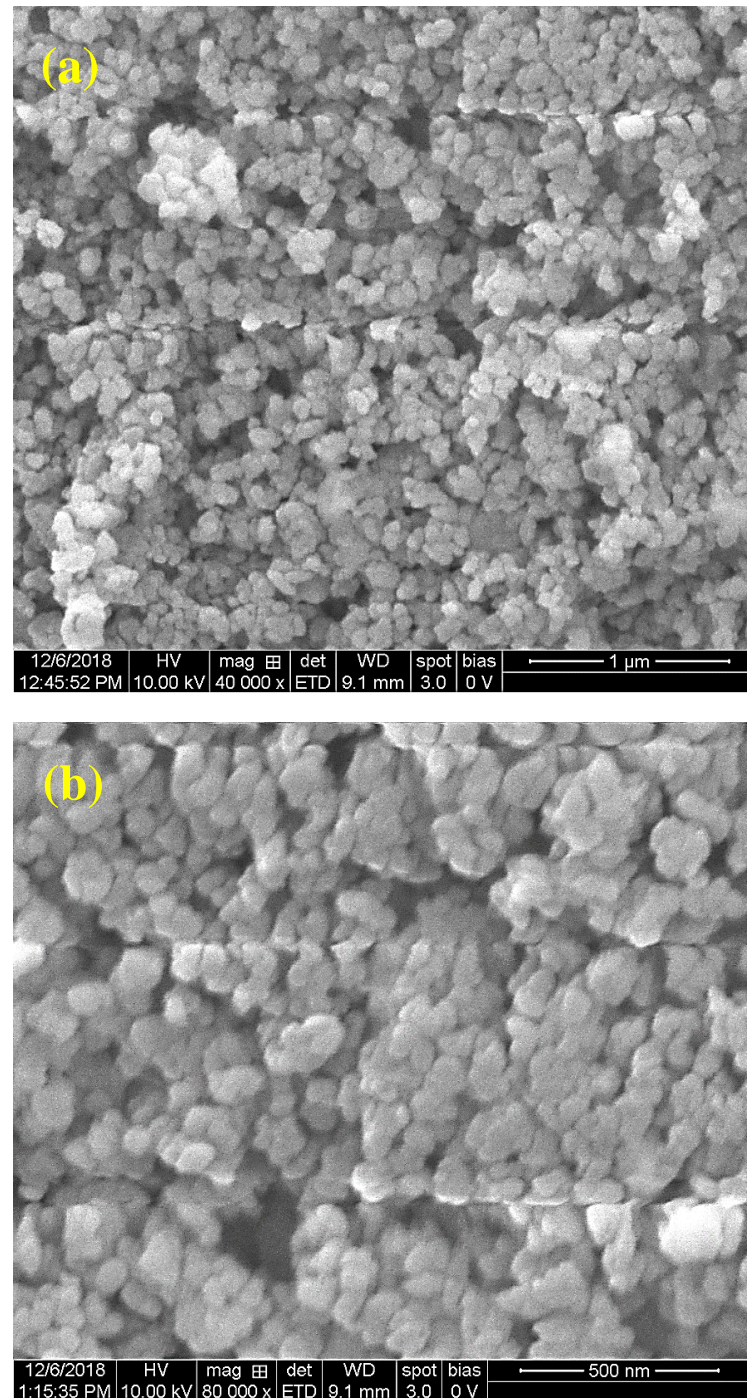

Figure 4. FESEM images of Ni^{2+}-doped HApNPs (**a**) 40,000×, (**b**) 80,000×.

3.5. EDAX Analysis

The EDAX spectrum (Figure 5) reveals the stoichiometric occupancy of Ca, O, Ni, and P, proving the synthesis of Ni^{2+}-doped HApNPs and ensuring that the models are in accordance with the HApNPs' fundamental ingredients and stoichiometry. The existence of P, O, Ca, and Ni may also be confirmed. The EDAX spectrum did not show any secondary phase or contamination signals. This sample elemental analysis confirmed the presence of Ca, O, P, and Ni in Ni^{2+}-doped HApNPs.
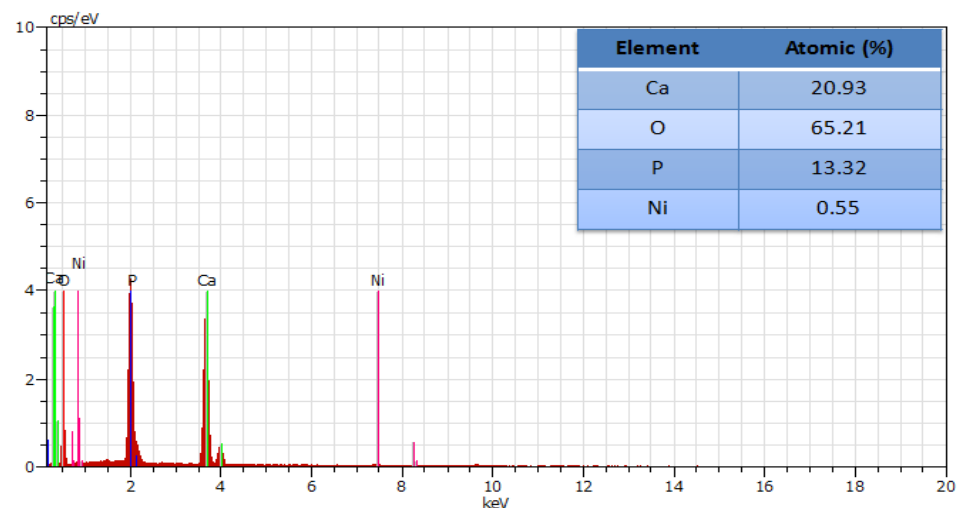

Element	Atomic (%)
Ca	20.93
O	65.21
P	13.32
Ni	0.55

Figure 5. EDAX spectrum of Ni^{2+}-doped HApNPs calcined at 500 °C.

3.6. PL Analysis

The PL emission spectra of Ni^{2+}-doped HApNPs synthesized through sol–gel synthesis are shown in Figure 6. The PL emission peaks of Ni^{2+}-doped HApNPs are located between 340 and 600 nm. Emission peaks were measured at 360, 376, 410, 494, 505, 520, 535, 572, 581, and 594 nm for the Ni^{2+}-doped HApNPs. Current research indicates that HAp and MOFE: HAp nanorods (NRs) have similar PL, with a wide visible emission band of about 310 nm. When UV light was applied to HApNPs, holes formed in the material that UV-induced trapholes might exploit, and both band gaps (5.2 and 5.5 eV) were also preserved [10].
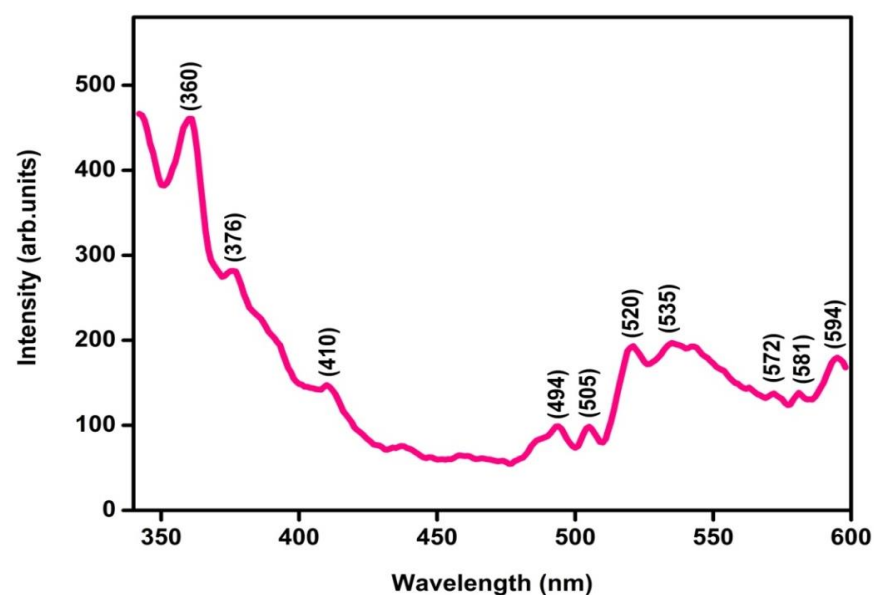

Figure 6. PL emission spectrum of Ni^{2+}-doped HApNPs calcined at 500 °C.

3.7. Antimicrobial Activity

3.7.1. Antibacterial Activity

Figure 7 shows the zone of the inhibitory effect of the five most prevalent pathogenic microorganisms. Furthermore, the optimal concentration was 50 g. Ni^{2+}-doped HApNPs were discovered to exhibit a maximum inhibition zone against *E. coli* of around 22 mm, demonstrating potent antibacterial action. The zone of inhibition shown by *P. aeruginosa* was rather large, measuring about 19 mm. The growth inhibitory impact of bacteria was modest against *S. flexneri* and *K. pneumoniae*. Minimal inhibitory zones were seen for *S. aureus* (Table 1). The finding demonstrates the high antibacterial activity of the produced Ni^{2+}-doped HApNPs. Similarly, a recent study [31] reported that Ni^{2+}-doped HApNPs showed remarkable antibacterial action against *E. coli* and *S. aureus*.
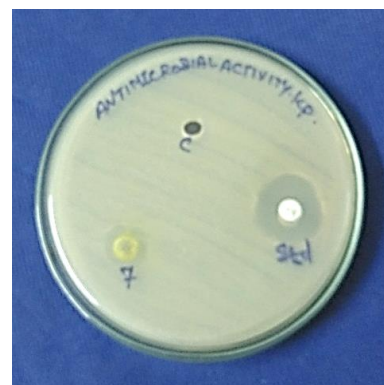

(a)

(b)

(c)

Figure 7. *Cont.*

(d)

(e)

Figure 7. Antibacterial activity of Ni²⁺-doped HApNPs treated against (**a**) *S. flexneri*, (**b**) *E. coli*, (**c**) *P. aeruginosa*, (**d**) *K. pneumoniae* and (**e**) *S. aureus.* C-Negative control (DMSO), Std.-Positive control (Amikacin), 7- Ni²⁺-doped HApNPs.

Table 1. Zone of inhibition of Ni²⁺-doped HApNPs against bacterial pathogens.

Samples	Zone of Inhibition (mm)					
	Shigella flexneri	*Escherichia coli*	*Pseudomonas aeruginosa*	*Klebsiella pneumonia*	*Staphylococcus aureus*	Negative Control
Ni²⁺-HApNPs	11	22	19	13	4	NZ
Amikacin	20	25	28	24	26	NZ

Positive control: Amikacin (30 µg), Negative control: DMSO, NZ- No Zone.

Bacterial inactivation is facilitated by ions in the NPs reacting with SH groups (proteins) [32]. They found a zone of restriction opposed to G⁻ᵛᵉ (14.9 0.97 mm) and G⁺ᵛᵉ (9.0 2.56 mm) bacteria, demonstrating that HApNPs' antimicrobial function can protect microorganisms [33]. Figure 8 depicts the mechanisms that contribute to the antibacterial effects of NPs. Possible mechanisms for the antibacterial effects of metal NPs include the absorption of free metal ions, which interfere with DNA replication, direct damage to cell membranes, reactive oxygen species (ROS), and the creation of ATP [34]. Well-diffusion pattern studies were used to investigate the antibacterial activity of AgNPs. In terms of maximal role containment, *Acinetobacter baumannii* (31 mm), *Staphylococcus aureus* (26 mm), and *Bacillus subtilis* (19 mm) were all successful [35]. The AgNPs were studied for their potential to inhibit DNA replication by interfering with bacterial membrane permeability processes [36].
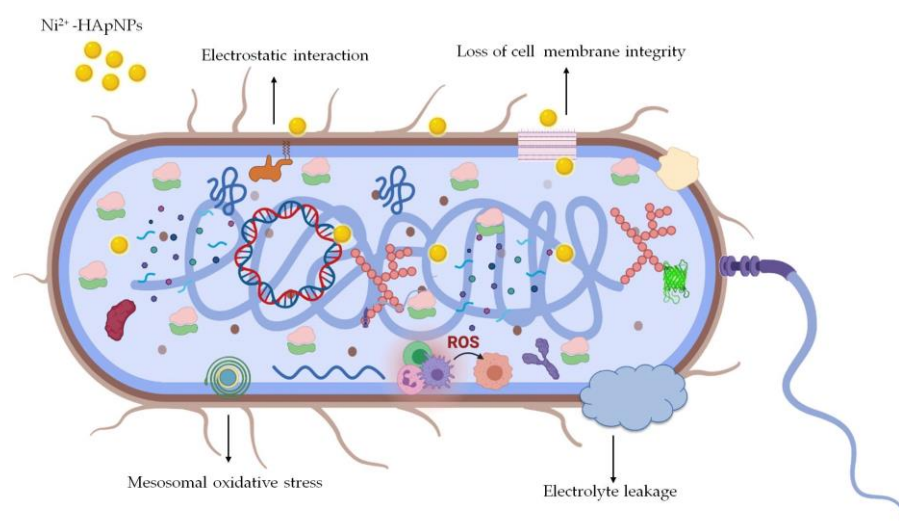
Figure 8. Illustration of the possible mechanism by which Ni^{2+}-doped HApNPs exert their antibacterial effects.

3.7.2. Antifungal Activity

Synthesized Ni^{2+}-doped HApNPs revealed antifungal activity with an inhibitory zone opposite that of *A. flavus*, *O. caricae*, and *A. niger* (Figure 9; Table 2). However, clotrimazole, a persistent antibiotic, had the greatest activity across all species tested. The antifungal activity also exhibited structure, with the highest activity at 50 g. The maximum inhibitory zone for Ni^{2+}-doped HApNPs was observed at a distance of 23 mm from *O. caricae*. The zone of inhibition for *A. flavus*'s growth was modest at 11 mm. *A. niger* exhibited a minimal inhibitory zone. Ni^{2+}-doped HApNPs were successfully produced, and the results verified their potent antifungal properties. Ag-HApNPs displayed antibacterial activity against *O. caricae*, *A. niger*, and *A. flavus*, with the zone of inhibition values of 27, 23, and 25 mm, respectively, as reported in our earlier studies [23].
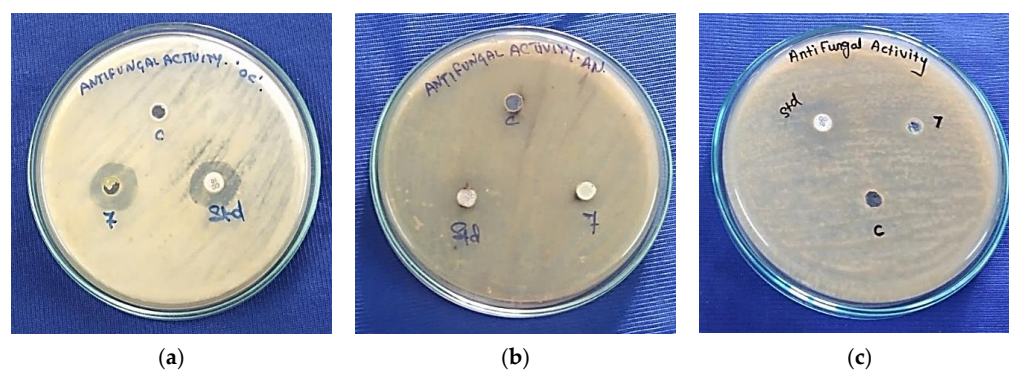

(**a**) (**b**) (**c**)

Figure 9. Antifungal activity of Ni^{2+}-doped HApNPs treated against (**a**) *O. caricae*, (**b**) *A. niger* and (**c**) *A. flavus*.

Table 2. Antifungal activity of Ni^{2+}-doped HApNPs treated against fungal pathogens.

Samples	Zone of Inhibition (mm)			
	Oidium caricae	*Aspergillus niger*	*Aspergillus flavus*	Negative Control
Ni^{2+}-HApNPs	23	5	11	NZ
Clotrimazole	29	21	25	NZ

Positive control: Clotrimazole (10 µg), Negative control: DMSO, NZ—No Zone.

3.8. Antioxidant Activity

Ni^{2+}-doped HApNPs antioxidant activity was tested using diphenyl phosphate (DPPH), and the results revealed that the free radical scavenging function of the HApNPs increased with increasing concentration (Figure 10). Ni^{2+}-doped HApNPs demonstrated superior scavenging performance. In contrast, standard Rutin only managed 60% efficiency over the whole concentration range (100 to 400 μg/mL). Thus, Ni^{2+}-doped HApNPs are the best option due to their superior antioxidant process. Studies using a similar design have connected the formulation's 1,1'-diphenyl-2-picrylhydrazyl and hydrogen peroxide scavenging capabilities to stable ascorbic acid, with the increased activity mainly related to the presence of phenols and flavonoids [37,38].
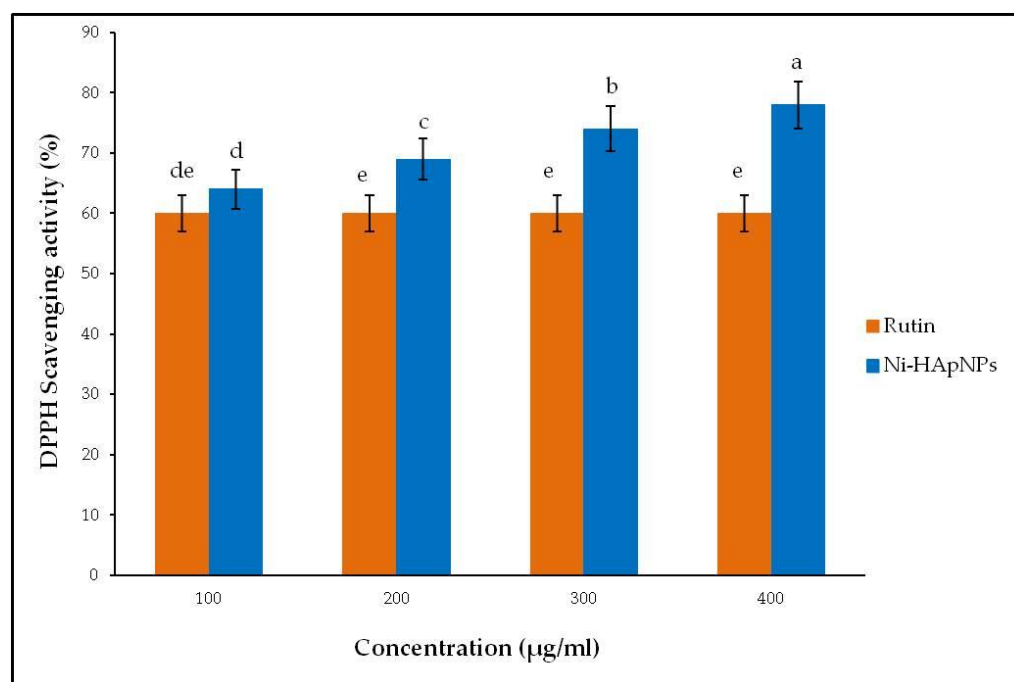

Figure 10. Antioxidant activity of Ni^{2+} doped HApNPs. Different letters above each column indicate significant differences (ANOVA, Tukey's HSD test, $p < 0.05$).

3.9. Anticancer Activity

The effect of Ni^{2+}-doped HApNPs on the growth and viability of HeLa cell lines was evaluated using the MTT assay (Figure 11; Table 3). Different concentrations of Ni^{2+}-doped HApNPs were investigated for this test to find an effective dose. When tested against HeLa cell lines, the Ni^{2+}-doped HApNPs sample significantly increased cytotoxicity. Size and cell type have a role in determining the cytotoxicity caused by NPs. At 100 μg/mL, Ni^{2+}-doped HAp had a cell viability of 32.19%, whereas Ni^{2+}-doped HApNPs had viability between 52.12 and 92.5% at 50, 70, and 6.25 μg/mL. Cell death occurred at a rate of 30%, even at a concentration of 100 μg/mL. In contrast to HeLa cell lines, the synthesized Ni^{2+}-doped HApNPs exhibited cytotoxicity as measured by the MTT assay, with an IC_{50} value of 68.82 μg/mL. Comparatively, silver nanoparticles (AgNPs) were shown to have strong anticancer activity against the breast cancer cell line MCF 7 [35]. CaO NPs exhibited apoptotic characteristics, including cell shrinkage and condensed and fragmented nuclei, in contrast to the cell proliferation structures of A549 cells observed in the previous research article [39].
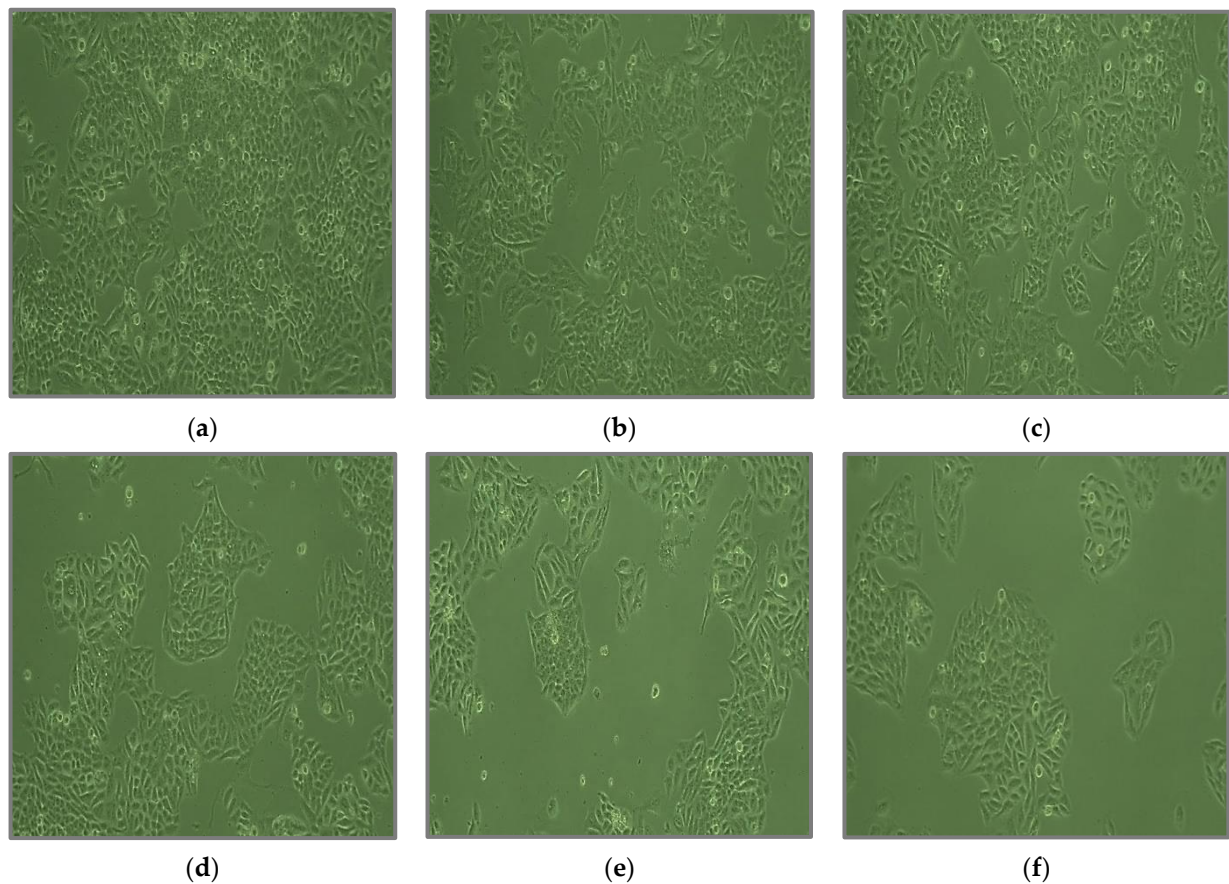
Figure 11. Anticancer activity of Ni^{2+} doped HApNPs. (**a**) control, (**b**) 6.25 µg/mL, (**c**) 12.5 µg/mL, (**d**) 25 µg/mL, (**e**) 50 µg/mL, (**f**) 100 µg/mL.

Table 3. Anticancer activity of Ni^{2+}-doped HApNPs tested on HeLa cells.

Sample	Cell Viability (%)					IC_{50} µg/mL
	6.25 µg/mL	12.5 µg/mL	25 µg/mL	50 µg/mL	100 µg/mL	
Ni^{2+}-HApNPs	92.55	81.99	73.40	52.12	32.97	68.817

4. Conclusions

The sol–gel method was used to synthesize Ni^{2+}-doped HApNPs. Ni^{2+}-doped HAp-NPs are shown to be nanocrystalline, as evidenced by their XRD pattern. Typically, a crystallite is about 39.91 nm in size. Functional groups like O-H and O-P-O are confirmed by FTIR and Raman spectroscopy. The EDAX confirmed Ni^{2+} ion doping in the HAp structure, and the FESEM examination showed the particles to be spherical or nearly spherical in shape. The sample shows significant agglomeration when Ni^{2+} ions are substituted for other cations. Ni^{2+}-doped HApNPs were shown to be very effective against various bacteria when tested using the disc diffusion technique, including *S. flexneri*, *E. coli*, *P. aeruginosa*, *K. pneumoniae*, and *S. aureus*. High levels of antifungal, antioxidant, and anticancer activity are seen in HApNPs doped with Ni^{2+}. As a result, the Ni^{2+}-doped HApNPs have potential in the biomedical sector for implantation in orthopedics and surgical procedures.

References

1. Banumathi, B.; Vaseeharan, B.; Ishwarya, R.; Govindarajan, M.; Alharbi, N.S.; Kadaikunnan, S.; Khaled, J.M.; Benelli, G. Toxicity of herbal extracts used in ethno-veterinary medicine and green-encapsulated ZnO nanoparticles against *Aedes aegypti* and microbial pathogens. *Parasitol. Res.* **2017**, *116*, 1637–1651. [CrossRef]
2. Monika, P.; Chandraprabha, M.N.; Hari Krishna, R.; Vittal, M.; Likhitha, C.; Pooja, N.; Chaudhary, V. Recent advances in pomegranate peel extract mediated nanoparticles for clinical and biomedical applications. *Biotechnol. Genet. Eng. Rev.* **2022**, 1–29. [CrossRef]
3. Ishwarya, R.; Vaseeharan, B.; Anuradha, R.; Rekha, R.; Govindarajan, M.; Alharbi, N.S.; Kadaikunnan, S.; Khaled, J.M.; Benelli, G. Eco-friendly fabrication of Ag nanostructures using the seed extract of *Pedalium murex*, an ancient Indian medicinal plant: Histopathological effects on the Zika virus vector *Aedes aegypti* and inhibition of biofilm-forming pathogenic bacteria. *J. Photochem. Photobiol. B Biol.* **2017**, *174*, 133–143. [CrossRef] [PubMed]
4. Kalaiselvi, V.; Mathammal, R.; Anitha, P. Sol-gel mediated synthesis of pure hydroxyapatite at different temperatures and silver substituted hydroxyapatite for biomedical applications. *J. Biotechnol. Biomater.* **2017**, *7*, 275.
5. Panneerselvam, R.; Anandhan, N.; Gopu, G.; Ganesan, K.P.; Marimuthu, T. Impact of different transition metal ions in the structural, mechanical, optical, chemico-physical and biological properties of nanohydroxyapatite. *Appl. Surf. Sci.* **2020**, *506*, 144802.
6. Pathania, D.; Sharma, M.; Thakur, P.; Chaudhary, V.; Kaushik, A.; Furukawa, H.; Khosla, A. Exploring phytochemical composition, photocatalytic, antibacterial, and antifungal efficacies of Au NPs supported by *Cymbopogon flexuosus* essential oil. *Sci. Rep.* **2022**, *12*, 1–15. [CrossRef] [PubMed]
7. Pathania, D.; Kumar, S.; Thakur, P.; Chaudhary, V.; Kaushik, A.; Varma, R.S.; Furukawa, H.; Sharma, M.; Khosla, A. Essential oil-mediated biocompatible magnesium nanoparticles with enhanced antibacterial, antifungal, and photocatalytic efficacies. *Sci. Rep.* **2022**, *12*, 1–13. [CrossRef]
8. Wei, G.; Ma, P.X. Structure and properties of nano-hydroxyapatite/polymer composite scaffolds for bone tissue engineering. *Biomaterials* **2004**, *25*, 4749–4757. [CrossRef] [PubMed]
9. Gayathri, B.; Muthukumarasamy, N.; Velauthapillai, D.; Santhosh, S.B. Magnesium incorporated hydroxyapatite nanoparticles, preparation, characterization, antibacterial and larvicidal activity. *Arabian. J. Chem.* **2016**, *11*, 645–654. [CrossRef]
10. Kalaiselvi, V.; Mathammal, R.; Vijayakumar, S.; Vaseeharan, B. Microwave assisted green synthesis of Hydroxyapatite nanorods using *Moringa oleifera* flower extract and its antimicrobial applications. *Int. J. Vet. Sci. Med.* **2018**, *6*, 286–295. [CrossRef] [PubMed]
11. Kaygili, O.; Dorozhkin, S.V.; Ates, T.; Al-Ghamdi, A.A.; Yakuphanoglu, F. Dielectric properties of Fe doped hydroxyapatite prepared by sol-gel method. *Ceram. Int.* **2014**, *40*, 9395–9402. [CrossRef]
12. Kaygili, O.; Keser, S. Zr/Mg, Zr/Sr and Zr/Zn Co-doped Hydroxyapatites: Synthesis and Characterization. *Ceram. Int.* **2016**, *42*, 9270–9273. [CrossRef]
13. Lala, S.; Maity, T.N.; Singha, M.; Biswas, K.; Pradhan, S.K. Effect of doping (Mg, Mn, Zn) on the microstructure and mechanical properties of spark plasma sintered hydroxyapatites synthesized by mechanical alloying. *Ceram. Int.* **2017**, *43*, 2389–2397. [CrossRef]
14. Yahia, I.S.; Shkir, M.; AlFaify, S.; Ganesh, V.; Zahran, H.Y.; Kilany, M. Facile microwave-assisted synthesis of Te-doped hydroxyapatite nanorods and nanosheets and their characterizations for bone cement applications. *Mater. Sci. Eng. C Mater. Biol. Appl.* **2017**, *72*, 472–480. [CrossRef] [PubMed]
15. Moreira, M.P.; De Almeida Soares, G.D.; Dentzer, J.; Anselme, K.; De Sena, L.Á.; Kuznetsov, A.; Dos Santos, E.A. Synthesis of magnesium- and manganese-doped hydroxyapatite structures assisted by the simultaneous incorporation of strontium. *Mater. Sci. Eng. C* **2016**, *61*, 736–743. [CrossRef]

16. Abdel Raouf, N.; Al-Enazi, N.M.; Ibraheem, I.B.M. Green biosynthesis of gold nanoparticles using *Galaxaura elongata* and characterization of their antibacterial activity. *Arabian J. Chem.* **2017**, *10*, S3029–S3039. [CrossRef]

17. Brand-Williams, W.; Cuvelier, M.E.; Berset, C. Use of a free-radical method to evaluate antioxidant activity Food. *Sci. Technol.-Lebensm.-Wiss. Technol.* **1995**, *28*, 25–30. [CrossRef]

18. Nomura, K.; Barrero, C.A.; Sakuma, J.; Takeda, M. Room-temperature ferromagnetism of sol-gel synthesized $Sn_{1-x}{}^{57}Fe_xO_{2-\delta}$ powders. *Phys. Rev. B* **2007**, *75*, 184411. [CrossRef]

19. Kazin, P.E.; Gazizova, O.R.; Karpov, A.S.; Jansen, M.; Tretyakov, Y.D. Incorporation of 3d-metal ions in the hexagonal channels of the $Sr^5(PO_4)3OH$ apatite. *Solid. State. Sci.* **2007**, *9*, 82–87. [CrossRef]

20. Baikie, T.; Ng, G.M.; Madhavi, H.; Pramana, S.; Blake, S.S.; Elcombe, K.M.; White, T.J. The crystal chemistry of the alkaline earth apatites A10(PO_4)6CuxOy(H)z (A=Ca, Sr and Ba). *RSC Dalton. Trans.* **2009**, *34*, 6722–6726. [CrossRef]

21. Govindarajan, M.; Benelli, G. A facile one-pot synthesis of ecofriendly nanoparticles using *Carissa carandas*: Ovicidal and larvicidal potential on malaria, dengue and filariasis mosquito vectors. *J. Clust. Sci.* **2017**, *28*, 15–36. [CrossRef]

22. Baranitharan, M.; Alarifi, S.; Alkahtani, S.; Ali, D.; Elumalai, K.; Pandiyan, J.; Krishnappa, K.; Rajeswary, M.; Govindarajan, M. Phytochemical analysis and fabrication of silver nanoparticles using *Acacia catechu*: An efficacious and ecofriendly control tool against selected polyphagous insect pests. *Saudi J. Biol. Sci.* **2021**, *28*, 148–156. [CrossRef]

23. Sebastiammal, S.; Fathima, A.S.L.; Alarifi, S.; Mahboob, S.; Henry, J.; Kavipriya, M.R.; Govindarajan, M.; Nicoletti, M.; Vaseeharan, B. Synthesis and physicochemical characteristics of Ag-doped hydroxyapatite nanoparticles, and their potential biomedical applications. *Environ. Res.* **2022**, *210*, 112979. [CrossRef]

24. Gopi, D.; Karthika, A.; Rajeswari, D.; Kavitha, L.; Pramod, R.; Dwivedi, J. Investigation on corrosion protection and mechanical performance of minerals substituted hydroxyapatite coating on HELCDEB-treated titanium using pulsed electrodeposition method. *RSC Adv.* **2014**, *4*, 34751–34759. [CrossRef]

25. Iafisco, M.; Ruffini, A.; Adamiano, A.; Sprio, S.; Tampieri, A. Biomimetic magnesium-carbonate-apatite nanocrystals endowed with strontium ions as anti-osteoporotic trigger. *Mater. Sci. Eng. C* **2014**, *35*, 212–219. [CrossRef]

26. Geng, Z.; Cui, Z.; Li, Z.; Zhu, S.; Liang, Y.; William Weijia, L.; Yang, X. Synthesis, characterization and the formation mechanism of magnesium and strontium-substituted hydroxyapatite. *J. Mater. Chem. B* **2015**, *3*, 3738. [CrossRef]

27. Junfeng, J.; Huanjun, Z.; Jie, W.; Xin, J.; Hong, H.; Fangping, C.; Shicheng, W.; Jung-Woog, S.; Changsheng, L. Development of magnesium calcium phosphate biocement for bone regeneration. *J. R. Soc. Interface* **2010**, *6*, 1171–1180.

28. Gerrard, E.; Jai, P.; Sridevi, B.; Suraj Kumar, T.; Mrutyunjay, S.; Derek, F. Kinetic and adsorption behaviour of aqueous cadmium using a 30 nm hydroxyapatite based powder synthesized via a combined ultrasound and microwave based technique. *Phys. Chem.* **2016**, *6*, 11–22.

29. Iafisco, M.; Morales, J.G.; Hernandez-Hernandez, M.A.; Garcia-Ruiz, J.M.; Roveri, N. Biomimetic carbonate–hydroxyapatite nanocrystals prepared by vapour diffusion. *Adv. Eng. Mater.* **2010**, *12*, B218–B223. [CrossRef]

30. Anu Priya, B.; Senthilguru, K.; Agarwal, T.; Narayana, S.G.H.; Giri, S.; Pramanik, K.; Pal, K.; Banerjee, I. Nickel doped nanohydroxyapatite: Vascular endothelial growth factor inducing biomaterial for bone tissue engineering. *RSC Adv.* **2015**, *5*, 72515–72528. [CrossRef]

31. Jenifer, A.; Sakthivel, P.; Senthilarasan, K.; Sivaprakash, P.; Arumugam, S. In Vitro Analysis of Nickel Doped Hydroxyapatite For Biomedical Applications. *Int. J. Sci. Technol. Res.* **2019**, *8*, 781–787.

32. Guzman, M.; Dille, J.; Godet, S. Synthesis and antibacterial activity of silver nanoparticles against gram-positive and gram-negative bacteria. *Nanomed. Nanotechnol. Biol. Med.* **2012**, *8*, 37–45. [CrossRef]

33. Ragab, H.S.; Ibrahim, F.A.; Abdallah, F.; Al-Ghamdi, A.A.; Tantawy, F.E.; Yakuphanoglu, F. Synthesis and in vitro antibacterial properties of hydroxyapatite nanoparticles. *J. Pharm. Biol. Sci.* **2014**, *9*, 77–85. [CrossRef]

34. Kumar, S.V.; Karpagambigai, S.; Rosy, P.J.; Rajeshkumar, S. Controlling of disease causing pathogens using silver nanoparticles synthesized by one step green procedure. *J. Appl. Pharm. Sci.* **2018**, *8*, 142–146.

35. AlSalhi, M.S.; Elangovan, K.; Ranjitsingh, A.J.A.; Murali, P.; Devanesan, S. Synthesis of silver nanoparticles using plant derived 4-N-methyl benzoic acid and evaluation of antimicrobial, antioxidant and antitumor activity. *Saudi J. Biol. Sci.* **2019**, *26*, 970–978. [CrossRef]

36. Korshed, P.; Li, L.; Liu, Z.; Wang, T. The molecular mechanisms of the antibacterial effect of picosecond laser generated silver nanoparticles and their toxicity to human cells. *PLoS ONE* **2018**, *13*, e0203636. [CrossRef] [PubMed]

37. Chaloupka, K.; Malam, Y.; Seifalian, A.M. Nanosilver as a new generation of nanoproduct in biomedical applications. *Trends Biotechnol.* **2010**, *28*, 580–588. [CrossRef]

38. Kumar, S.A.; Prabhakar, R.; Vikram, N.R.; Dinesh, S.P.S.; Rajeshkumar, S. Antioxidant Activity of Silymarin/Hydroxyapatite /Chitosan Nano Composites-An In Vitro Study. *Int. J. Dent. Oral. Sci.* **2021**, *26*, 1402–1404. [CrossRef]

39. Yoonus, J.; Resmi, R.; Beena, B. Greener nanoscience: Piper betel leaf extract mediated synthesis of CaO nanoparticles and evaluation of its antibacterial and anticancer activity. *Mater. Today Proc.* **2020**, *41*, 535–540. [CrossRef]